Materials Chemistry and Physics 327 (2024) 129834

Contents lists available at ScienceDirect

Materials Chemistry and Physics

journal homepage: www.elsevier.com/locate/matchemphys

Synthesis and electrochemical characteristics of metal nanoparticles decorated composite anode made of domestic alloy, used in lithium ion batteries

Mehmet Feryat Gülcan [a], Billur Deniz Karahan [a,b,*]

[a] Department of Metallurgical and Materials Engineering, Istanbul Technical University, Ayazaga Campus, 34469, Istanbul, Turkey
[b] Istanbul Medipol University, Research Institute for Health Sciences and Technologies (SABITA), 34810, Beykoz, Istanbul, Turkey

HIGHLIGHTS

- A domestic FeCr alloy is used as raw material instead of synthetic chemicals.
- Composition and structure are optimized to form low-C footprint composite electrode.
- Metal nanoparticles create conductive pathways for high-rate performance.
- The electrode delivers 750 mAh g^{-1} at the 300th cycles.

GRAPHICAL ABSTRACT

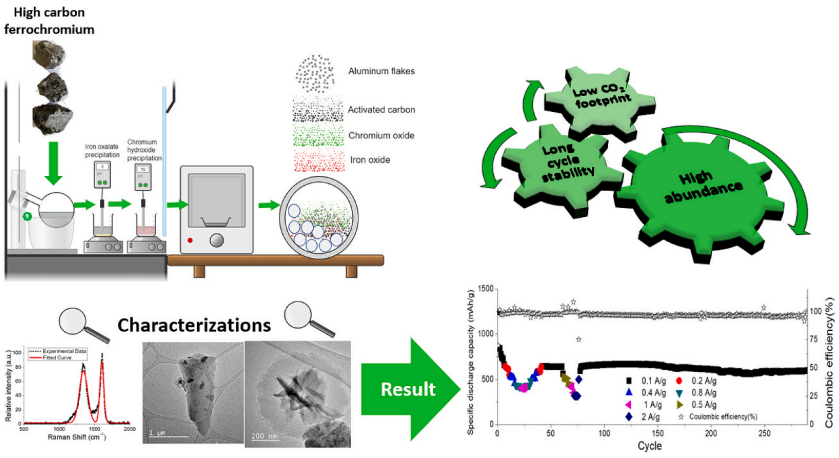

ARTICLE INFO

Keywords:
Low-carbon footprint anode for LIB
Mechanochemical synthesis
Metal oxide composite
Ball milling

ABSTRACT

In this work, appropriate material selection and process design enable the succesful production of high energy density electrode active material in the form of XAZ (where X, A and Z stand for electrochemically active, electrochemically inactive and carbon materials, respectively). Herein, the precipitates rich in iron and chromium are extracted selectively from a local ferrochromium alloy utilizing hydrometallurgy procedures. The precipitates are then exposed to separate calcination to get iron-rich and chromium-rich oxides seperately. In the end, a composite (XAZ) is fabricated under the mild synthesis conditions by combining these oxides with activated carbon and aluminum powder in a planetary ball mill. The composite's morphological, structural, and chemical properties are all optimized. The galvanostatic test results clearly demonstrate that the powder made of XAZ composite with embedded metal nanoparticles delivers 798 mAh g^{-1} after 100th cycle under a current load of 50 mA g^{-1} and high capacity (600 mAh g^{-1}) over 300 cycles with an exceptional rate performance. It is

* Corresponding author. Department of Metallurgical and Materials Engineering, Istanbul Technical University, Ayazaga Campus, 34469, Istanbul, Turkey.
E-mail address: bdkarahan@itu.edu.tr (B.D. Karahan).

https://doi.org/10.1016/j.matchemphys.2024.129834
Received 5 April 2024; Received in revised form 28 July 2024; Accepted 6 August 2024
Available online 14 August 2024

anticipated that this research will create novel opportunities for producing high-value electrode active materials from accessible, low-cost raw ingredients.

1. Introduction

Due to the quick development of electric vehicles (EVs), lithium-ion batteries (LIBs) are in high demand. Further mining will therefore be required to create electrode active materials for batteries because it is expected that the global LIB demand would reach 1293 GWh by 2030 [1]. Moreover, recent advances in technology requires high energy density batteries. This has paved the way for research on the production of environmentally friendly electrode active materials with higher capacities. Therefore, by considering the high energy demand of the electrode production methods and the emissions caused by the fossil fuel (primary energy source used in the fabrication) a need for alternative solutions is urged to ensure sustainable battery production.

The analysis shows that the anode active materials used in lithium-ion batteries (LIBs) may follow different reaction mechanisms in cycling: intercalation, conversion, and alloying. Those materials (i.e. C based materials [2]) performing intercalation-type reactions with Li, they have stable structures and long cycle life, but low capacity due to their redox operation and structural properties [3]. And, the materials performing conversion type reactions deliver high reversible capacity but poor rate performance due to their low conductivity [2]. Finally, materials which form alloy with lithium have the highest practical capacity but low capacity retention due to serious volume expansion problems [4]. Among them, transition metal oxides performing conversion reaction as a negative electrode material with a theoretical capacity of over 700 mA h/g, face challenges as commercial LIBs anodes due to their semiconductor behavior that limit its cycle performance [4–7]. Nanoengineering transition metal oxides are a successful strategy for reducing Li^+ diffusion time to the core, hence improving rate capabilities [8,9]. Those made of iron oxide/chromium oxide mixtures or chromium ferrite attract attention. They all exhibit significant capacity loss and low initial coulombic efficiency during cycling, despite the fact that their capacities are consistently greater than those of graphite. For instance, Mumtaz et al. study [10] found a 60 % loss in the (MWCNTs)/$CrFe_2O_4$ composite after 100 cycles. Then, in Harpak et al work, a 50 % capacity loss at 0.25C was noted in the stainless steel composite after 200 cycles [11]. To further increase the cycle performance of metal oxides, decoration with nano-sized metals has been proposed. Nano-sized metal decoration provides advantages for reaching capacities at high currents loads or increasing the capacity conservation over cycling. Such performance is achieved by both increasing the conductivity of the electrode [12] and lithiation mechanism [13]. Wu et al. [13] coated Ag nanoparticles on Cu foam to increase the capacity retention. Then, Guo et al. [14] decorated MnO_2 with Au. The material not only allowed for quick diffusion of ions and electrons due to its broad contact surface, but also served as a 3D current collector, offering excellent electrical conductivity and coulombic efficiency [14]. Then Cheng et al. [15] added nano copper particles to LTO material, to achieve higher capacity performance even at high current loads. Moreover, aluminum which forms alloy with Li could be a potential candidate to be used as anode active material in lithium-ion batteries [16]. However, its use is problematic due to its structural instability. Additionally, it is known that aluminum is present in nature with its oxide surface layer, which is an insulator material [17] causing higher impedance when it is being directly used as electrode active material.

Therefore, fabricating composite electrode material with a decoration of nano-sized metal particles stands out [18,19] since by composite formation both the capacity and the cycle life could be optimized and by means of nano-sized metal decoration the rate performance and the capacity retention are expected to be improved. The composite basically consists of an electrochemically active compound along with an inactive one that conducts electrons. Such a design improves the stress accommodation ability of the electrode material [20]. In order to promote the rate performance capability of the electrode active material, metallic nanoparticles and/or carbon atoms may be embedded in the material. Therefore, to combine both capacity with rate performance capability, a composite made of XAZ structure is proposed, where X, A and Z stand for electrochemically active material, electrochemically inactive material and carbon, respectively. Using the same rational method, different scientists fabricated anode active material with remarkable electrochemical performances (i.e. *Si*-Cu_3Si-Al_2O_3 [20], SnSb-TiC-C [21], $FeSb_2-Al_2O_3-C$ [22], $NiSb-Al_2O_3-C$ [23] and $Cu_2Sb–Al_2O_3–C$ [24]). In their fabrication, mostly, high-purity metal salts were used as starting material, resulting in an increase in the cost as well as the C-footprint of the resulting products.

This article suggests an alternate method for producing a sustainable anode active material (AAM) for lithium-ion batteries. For the first time in the literature, using a locally produced ferrochromium (FeCr) alloy as a starting material, the production of XAZ composite material and its use as AAM is investigated. Turkiye produced 94,000 tonnes of ferrochromium in 2015 [25]. Use of domestic product in the synthesis reduces carbon dioxide emissions associated with transportation of the raw material and lowers the raw material supply chain risk. Furthermore, different concentrations of trace transition metals found in high carbon ferrochromium may have a combined effect on the electrochemical performance of AAM.

In our previous studies [26,27] first the leaching of FeCr by sulfuric acid was optimized [26], then from this leachate iron oxides of different structures were produced selectively [27] to be used as AAM in LIB. In the present study, by using a domestic product as the starting material, it is intended to reduce both the carbon dioxide released during the production of a primary quality raw material to be used in the production of electrode materials as well as the carbon dioxide released during the transportation of the raw material obtained in other locations. Accordingly, a novel flow chart is designed to fabricate iron-rich and chromium-rich oxides containing powders from FeCr alloy (Fig. 1). Unlike the case of synthetic production methods, upon the fabrication of iron oxide powders from FeCr alloy, Mn and Co are entrapped in the iron oxide structure to create electron conductive pathways in the powder [27,28]. Moreover, as iron oxide and chromium oxide have been recognized as electrochemically active vs Li, using their mixture (as X in the XAZ formula) adds a new positive perspective to the study. For A (in XAZ), alumina is selected as inactive compound to act as a mechanical buffer. In the present setup, instead of adding Al_2O_3 directly into the composite, metallic aluminum is added into the mixture of metal oxide and the mixture is planetary ball milled together. Due to the high oxidation tendency of metallic aluminum, a mechanochemical synthesis is realized as it is processed with metal oxide under appropriate conditions. Khodaei et al. [29] mentioned that when aluminum was milled under an argon atmosphere with a metal oxide, without giving any heat to the system, the mechanical energy created in the vial triggered the reduction reaction of metal oxide to produce metallic nanoparticles along with alumina. In 2016, Allcorn and Manthiram [23] claimed that in ball milling, addition of carbon (C) in the vial promoted the reduction of metal oxide. Moreover, carbon having low voltage profile contributes to the energy storage capacity of AAM [23]. Therefore, for Z (in XAZ) carbon is added to the vial. Carbon together with the metallic nanoparticles formed as a result of the reduction reaction represent electron-conducting pathways in the composite powder. Moreover, their existences reduce the destructive effect of volume change in the anode structure.

Research on electrode design with high energy density and low carbon footprint has received a lot of attention lately. Knowing that so many factors need to be considered, no perfect design has been identified as of yet. In this study, an alternative solution to the existing problem is proposed by fabricating metal nanoparticles embedded in a XAZ structured composite via planetary ball-milling. The electrochemical performance of the composite powder is maximized through the optimization of the milling conditions. After 100 cycles, the electrode known as AADC displayed 798 mAh g^{-1} under a current load of 50 mA g^{-1}. The rate performance tests further revealed that the electrode (AADC) accomplished the cycle test even when it was subjected to high current loads (up to 2 A g^{-1}) and displayed a capacity of 600 mAh g^{-1} at the 300th cycle when tested under a current load of 100 mA g^{-1}.

2. Experimental

2.1. Materials

High carbon ferrochromium alloy is supplied from Eti Krom-Elazığ, Turkiye. Sulfuric acid and oxalic acid are purchased from Merck (1.00713.2500) and Isolab (LS096211DAGW), respectively. Deionized water, active carbon, and ammonium hydroxide are analytical grades. Stearic acid is purchased from Akbel Kimya and metallic aluminum is supplied from Nanokar (In Figs. S1a–b, the structural and morphological properties).

2.2. Powder fabrication

The novel chart designed for this study is given in Fig. 1.

2.2.1. Production of powder containing iron oxide

The optimization of the ferrochromium's leaching conditions and the concentration of the leachate were reported in our previous study [26]. In this paper, this leachate is used to fabricate iron oxide and chromium oxide, subsequently. First, oxalic acid is added to the leachate (1:5 volumetric ratio), and iron oxalate hydrate is precipitated selectively at pH 3 by using NH_4OH (14.53 M) at room temperature. This hydrous iron-rich oxalate powder is collected by centrifuge, dried at 70 °C (under vacuum) overnight, and heat treated at 300 °C for 2 h in an air atmosphere. The calcined powder is identified as FeO.

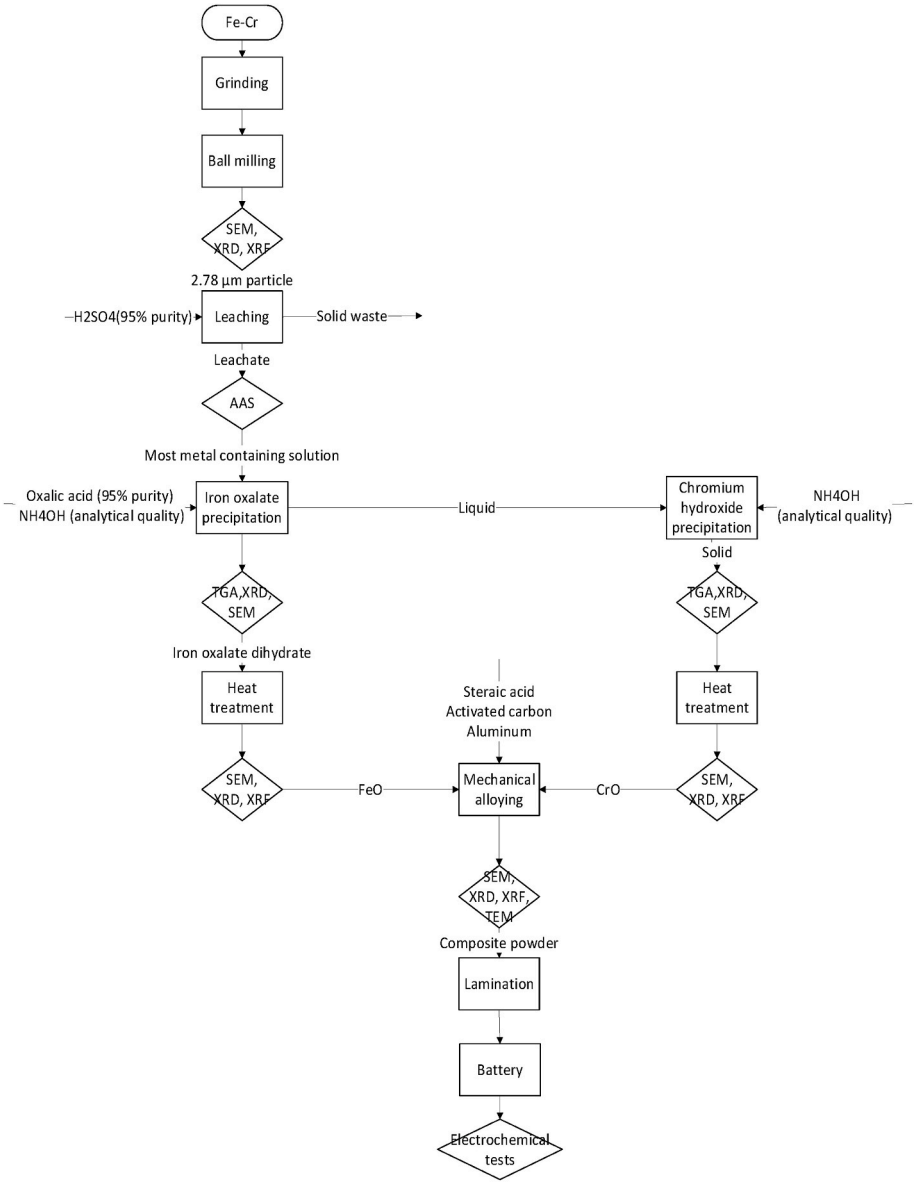

Fig. 1. Flow chart.

2.2.2. Production of powder containing chromium oxide

After the recovery of iron oxalate, the residual leachate is stirred magnetically at 200 rpm in room temperature while the pH is adjusted to 10 with NH_4OH (14.53 M). Following stirring for 30 min at this pH, the solution is aged for 3 days at room temperature for crystallization. The chromium-containing precipitate (Cr-P) is dried and heat treated at 430 °C for 1 h. The calcined chromium powder is labeled as CrO.

2.2.3. Production of composite powder

Planetary ball milling (Retsch PM100) is used in the fabrication of the composite. 2.87 g FeO, 1.43 g CrO, 1.05 g Al and 1.35 g activated carbon are measured and put in the vial. Stearic acid (%1.5 wt of the mixture) is also added to disperse the mixture in the vial and decrease the destructive effect of heating in milling.

One pot milling is performed with the following parameters in a partial argon atmosphere when all the above-mentioned four compounds are placed in a vial together: 300 rpm, 5 h (20 min run 10 min off), 20:1 ball to powder ratio, and vol%7 vial filling ratio. The obtained powder is labeled as AADC.

Three additional experiments are also conducted to investigate the effect of composition on the electrochemical performances: the first mixture is realized to get AADC without carbon (named as 'AAD'), the second mixture is produced to have AADC without chromium oxide (labelled as 'FeDC') and the third mixture merely contains aluminum and carbon (marked as 'AlC') without FeO and CrO (see Table 1 for sample coding). The performances of these additional electrodes are used to obtain complimentary information about the electrode active material's reaction mechanism with lithium.

2.3. Material characterizations

X-Ray Fluorescence (XRF) analyses are performed via Rigaku SUPERMINI 200 WDXRF. X-Ray Diffraction (XRD) analyses are made between $2\theta = 10–90^{\circ}$ with 0.02 step size via Bruker D2phaser. The morphological analysis is accomplished by FE-SEM (Zeiss Gemini 500). Particle size is measured by Malvern Panalytical, Zetasizer Ultra. Raman spectroscopy is completed with Renishaw (532 nm wavelength). Transmission Electron Microscopy (TEM) analysis is realized by JEOL JEM-ARM200CFEG UHR-TEM with 200 kV.

2.4. Electrochemical tests

The slurry contains 80 wt% active powder (AlC, FeDC, AADC, AAD), 10 wt% PVDF (MTI HSV900) and 10 wt% Super P conductive (TIMCAL) dissolved in NMP. Thinky ARE250 is used to stir the mixture. Dr. Blade is used to form electrodes onto 15 μm thick copper foils. Laminations are cold-rolled to achieve a thickness of less than 30 μm after being dried at 120 °C for 16 h in vacuum. The active material mass loading is 0.4 mg/cm^2 in average for all the fabricated electrodes.

CR2032 coin-type half-cells are assembled in an argon-filled glovebox (MBRAUN, Labmaster; H_2O 0.1 ppm O_2 0.1 ppm) to examine the electrochemical performances of the electrodes. Each cell contains a working electrode, a counter electrode (Li metal foil), a separator (Celgard 2400), and an electrolyte (Merck's Battery Grade electrolyte solution, 1 M $LiPF_6$ dissolved in EC:DMC 1:1). Each electrode's cycling stability is evaluated between 50 mV and 3 V (vs Li/Li$^+$) under a load of 50 mA g^{-1}. The electrodes are then tested under various current loads (from 100 mA g^{-1} to 2 A g^{-1}) to assess the changes in their capacities under high current loads.

Gamry Interface 1000E is used to obtain the first four cycles of the cyclic voltammograms (CV) and electrochemical impedance spectra (EIS) of the electrodes after the 1st and 10th cycle at 50 mV are taken in half cells. CV curves between 50 mV and 3 V (vs Li/Li$^+$) are obtained at a scan rate of 0.1 mV s^{-1}. EIS spectra are taken with AC amplitude of 1 mV once the electrode is discharged down to 50 mV and polarized at that potential for 9 h to get a stable electrode/electrolyte interface. Nyquist plots are recorded in the frequency range of 100 kHz to 0.01 Hz after 1st and 10th discharge reactions. Using the Gamry Echem Analyst software, the impedance data are fitted to the appropriate equivalent circuits.

Table 1
Sample coding and properties given in the manuscript.

Sample coding	Al	C	FeO	CrO
AADC	+	+	+	+
AAD	+	–	+	+
FeDC	+	+	+	–
AlC	+	+	–	–

3. Results and discussions

3.1. Structural and morphological characterizations

3.1.1. Powders recovered from FeCr alloy

In our previous work, the XRF result of the 5%-carbon-contained FeCr alloy was reported and its leaching with sulfuric acid was optimized [26]. In a previous study of our group, the oxalate precipitation method for the selective recovery of iron and iron group metals, excluding chromium, from this leachate was also reported [27]. There, this oxalate dihydrate underwent heat treatment at 180 °C and 550 °C in various atmospheres to produce porous iron-rich metal oxide powders.

Taking into consideration the results obtained from our previous research, in this work, to produce XAZ composite, the metal oxide powder is fabricated from FeCr alloy. In the present work, dihydrate oxalate is precipitated at pH 3 then vacuum dried (70 °C 12 h) and heated to 300 °C for 2h in air to transform the oxalate dehydrate to α-Fe_2O_3 (hematite), as discussed by Rao et al. [30]. XRD analysis confirms that the crystal structure of the sample (identified as FeO) is converted to hematite at the end of the heat treatment (Fig. 2a). SEM analysis reveals that FeO has columnar morphology (Fig. 3a) as defined by Dhal et al. [31].

The remaining leachate (rich in chromium) is treated by NH_4OH, and the pH of the solution is fixed to 10 to precipitate the chromium complex eventually. After stirring at 200 rpm for 3 h, the solution is left for aging over 48 h. As a result of this procedure, the efficiency of chromium recovery is found to be 86.9 % (Supp file defines the calculation method). Literature reveals that using transition metal sulfate in the electrode may have benefits in the cycle performance as their existence helps to control the volumetric expansion and improve the reaction kinetic [32]. Metal sulfates could also reversibly contribute to capacity [32]. Moreover, studies reveal that by adjusting the calcination temperature and duration in air, it is possible to produce various chromium phases with different Cr/O stoichiometries [33,34]. Of these oxide structures, Cr_3O_8 and Cr_2O_5 are frequently used as electrode materials since the distance between the layers in the structures is enlarged due to the presence of chromium in different valences. Therefore, Li can lithiate/delithiate easily in the structure [35,36]. Hence, the precipitate rich in chromium is heat treated at 430 °C for 1 h to obtain different stoichiometric phases together with chromium oxide and chromium sulfate [33,34] (Fig. 2b). SEM analysis reveals that the powder named as CrO has hexagon-shaped particles (Fig. 3a). This is in agreement with the findings of Liu et al. [36].

The chemical compositions of both FeO and CrO powders are examined by XRF (Table 2). Results show that selective recovery of Cr is achieved by pH adjustment and in the fabrication of FeO, not only Fe but also Ni, Co and Mn are precipitated with success, as expected. The sulfur in the chromium structure is associated with the chromium sulfate in the precipitate (Supp. Fig. S2a: Cr-P XRD result).

3.1.2. Composite by ball milling

The mechanochemical processing of metal oxide has become a subject of particular interest in recent years. There are various examples in

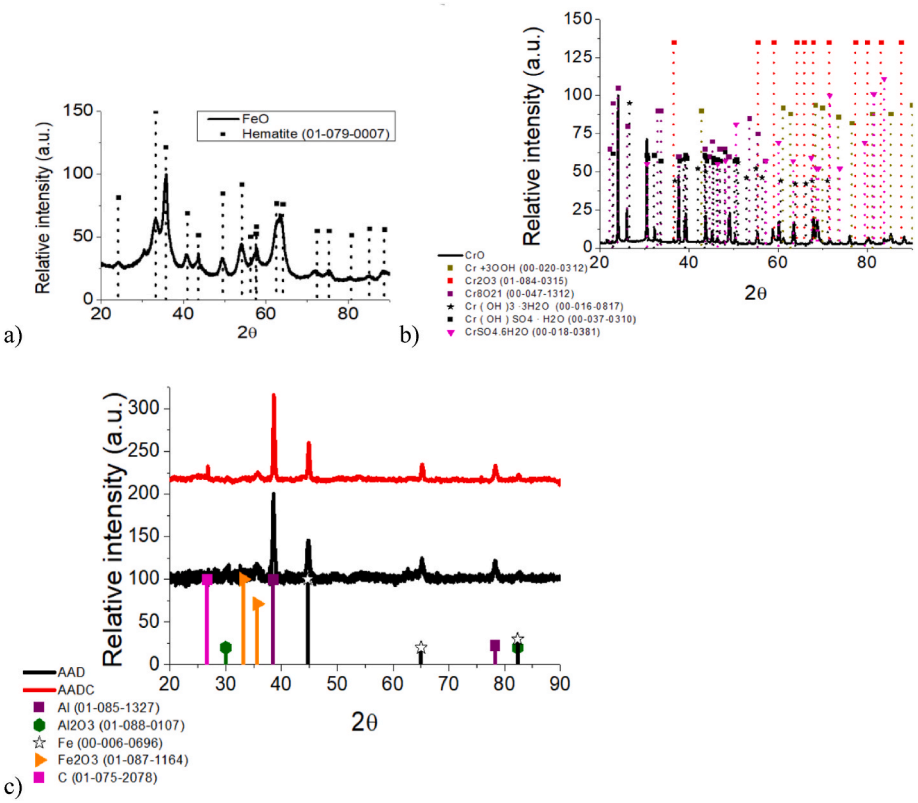

Fig. 2. XRD analysis a) FeO, b) CrO, c) AAD and AADC.

the literature regarding the use of this method in electrode synthesis for battery applications[37–40]. However, no study is found on the production of electrodes by mechanochemical processing of FeO and CrO mixtures, as proposed in the present paper.

De Souza and De Lemos [41] have ball-milled hematite with metallic aluminum powders to reduce hematite to iron by mechanochemical conversion reaction (see Eq. (1)). Different than conventional high energy conditions such transformation is only realized in a shorter time (5 h), with a speed of 300 rpm by using a planetary ball mill [42]. Therefore, in this study, firstly the powders recovered from FeCr alloy (FeO and CrO) are mixed with aluminum following Mojarrad et al.'s suggestion. This sample is labeled as AAD (see Table 1). XRD analysis of AAD shows the existence of Al_20_3, Al, transition metal (i.e. Fe) and transition metal oxide (i.e. Fe_2O_3) in the powder. This verifies that metal oxide is partially reduced forming metal and alumina (Fig. 2c), eventually. SEM images of AAD reveal that particles have irregular morphologies (Fig. 3c).

Then, Allcorn, Manthiram, Applestone et al. claim the positive effects of carbon in mechanochemistry due to its contribution to the reduction of metal oxides to sustain better retention in electrode capacity [22,24] (Eq (2)–(5)). In their studies, they state that these composites [43] exhibit superior ionic/electronic conductivities [43]. Thus, in this study, carbon are added to the mixture of FeO, CrO and Al (using the same experimental conditions for AAD), forming AADC eventually (see Table 1).

When we compare the particle size of AAD (without carbon) and AADC (with carbon) (Fig. 3e), AADC demonstrates lower particle size compared to AAD. Jia et al. [44] explained that less agglomeration occurred due to the existence of activated carbon in milling. SEM image demonstrates that AADC contains small-sized particles of irregular morphology, which tend to get together partially due to their high surface area.

When the XRD of AADC is studied in comparison to AAD, it is noted that the intensities of transition metal and alumina peaks increase, and the intensities of transition metal oxide peaks decrease (Fig. 2c). Kashiwaya and Ishii [45] have stated in their study that as a result of ball milling hematite with carbon in air and argon atmosphere, the oxidation level of iron changes and metallic iron can be formed. The reduction reactions that may take place are given in Eq. (2)–(5) [45].

$$Fe_2O_3 + x.Al \rightarrow 2Fe + y.Al_2O_3 + (x - 2.y)Al \quad (1)$$

$$3Fe_2O_3 + C \rightarrow 2Fe_3O_4 + CO \quad (2)$$

$$Fe_3O_4 + C \rightarrow 3FeO + CO \quad (3)$$

$$FeO + C \rightarrow Fe + CO \quad (4)$$

$$Fe_3O_4 + 4C \rightarrow 3Fe + 4CO \quad (5)$$

Then to differentiate the effect of CrO on AADC structure, FeO recovered from FeCr alloy is ball milled with Al and C in the same conditions (See Table 1). This sample is labeled as FeDC. XRD shows that in comparison to AADC, FeDC reveals lower peak intensities (Fig.S2b, $2\Theta = 32.6°$).

Finally, to differentiate the effect of transition metal oxide on AADC structure, none of the material recovered from FeCr alloy is used, instead Al and C are ball milled in the same conditions (see Table 1). This sample is named as AlC. XRD shows that in comparison to AADC, AlC (Fig.S2c) reveals no peak related to oxide formation which means alumina is only formed after the mechanochemical reaction of the transition metal oxide with aluminum.

To get more detailed information on AADC, Transmission Electron Microscopy (TEM) analysis is performed. Rod-shaped and spherical morphologies draw attention in accordance with SEM images (Fig. 3). In order to examine these particles in more detail, EDX analysis is performed (Fig. S3). As a result of EDX analysis, it is seen that the rod-shaped particle seen in Fig. 4a-b contains a high amount of carbon along with Al, O, Fe, S, Co, Cr (Fig. S3a.). Then Fig. S3a reveals that rod

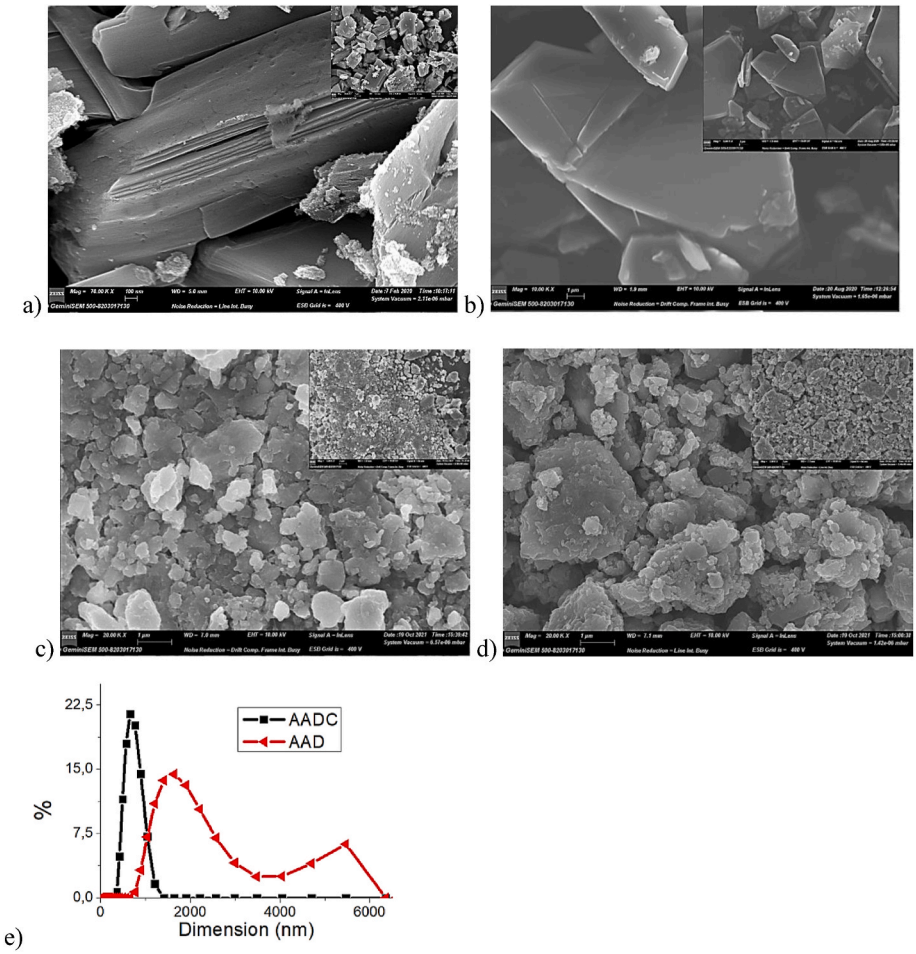

Fig. 3. SEM images a) FeO b) CrO c) AAD d) AADC. e) Particle size analysis of AADC and AAD.

Table 2
XRF (%wt) results for FeO and CrO.

	Al	S	Ca	Fe	Cr	Ni	Mn	Co
FeO	0.0905	0.3719	0	93.1516	3.4860	1.8738	0.2234	0.1535
CrO	0.1283	22.330	0.0473	5.3314	72.1631	0	0	0
AAD	13.315	17.67	0	25.075	9.61	0.51	0.115	0.03

shape particle is mainly made of C. When the spherical particles are studied, metallic Al is found to be embedded in an amorphous matrix (Fig. 4g and h). EDX mapping results indicate the presence of Fe-Co-Mn-O-containing structures in the Al_2O_3 matrix (Fig. S3b). This can be interpreted as the synthesis of amorphous Al_2O_3 - carbon matrix transition metal-containing electrode material, similar to the study of Allcorn and Manthiram [22,23] as a result of the experiment.

For further characterization of carbon in the structure, Raman analysis is realized (Fig. 5). In case of AADC, 2 peaks (1339 cm^{-1} and 1608 cm^{-1}) are recognized which are related to D and G-bands of carbon, respectively [46].

3.2. Electrochemical analysis

Wu et al. [47] reported that along with high capacity (around 1000 mAh g^{-1}), the transition metal oxides perform high volumetric changes (>200 %) leading to poor structural stability, hence weak cycle performance (Eq (6)–(8)) [47].

$$3Li + 1/2Fe_2O_3 \leftrightarrow 3/2Li_2O + Fe \quad (6)$$

$$8Li^+ + 8e^- + Fe_3O_4 \rightarrow 4\,Li_2O + 3Fe \quad (7)$$

$$4\,Li_2O + 3Fe \leftrightarrow 2\,LiFeO_2 + Fe + 6Li^+ + 6e^- \quad (8)$$

On the basis of the galvanostatic tests results, the potential applications of these powders as anode active materials for LIBs have been assessed. According to the galvanostatic performance, AAD delivers 1353.75 mAh g^{-1} as the 1st discharge capacity, and the capacity retention over 100 cycles is equal to %~17 compared to 1st discharge. The sample without chromium oxide (FeDC) performs 561.94 mAh g^{-1} capacity at 1st discharge and retains 339.43 mAh g^{-1} capacity after 100 cycles. The electrode made of AADC delivers the best performance as its first discharge capacity is noted to be 1824.13 mAh g^{-1}, and it retains ~ %44 of its initial capacity after 100 cycles. The difference between AADC and FeDC is the clue of the capacity contribution of CrO in the anode performance. When the galvanostatic performance of AlC with AADC is compared, the capacity retention seems to be very low for AlC and the electrode delivers <200 mA h/g after 20th cycles. This confirms that the inactive phases in the AADC structure (i.e. Al_2O_3) support the mechanical integrity of the electrode upon cycling.

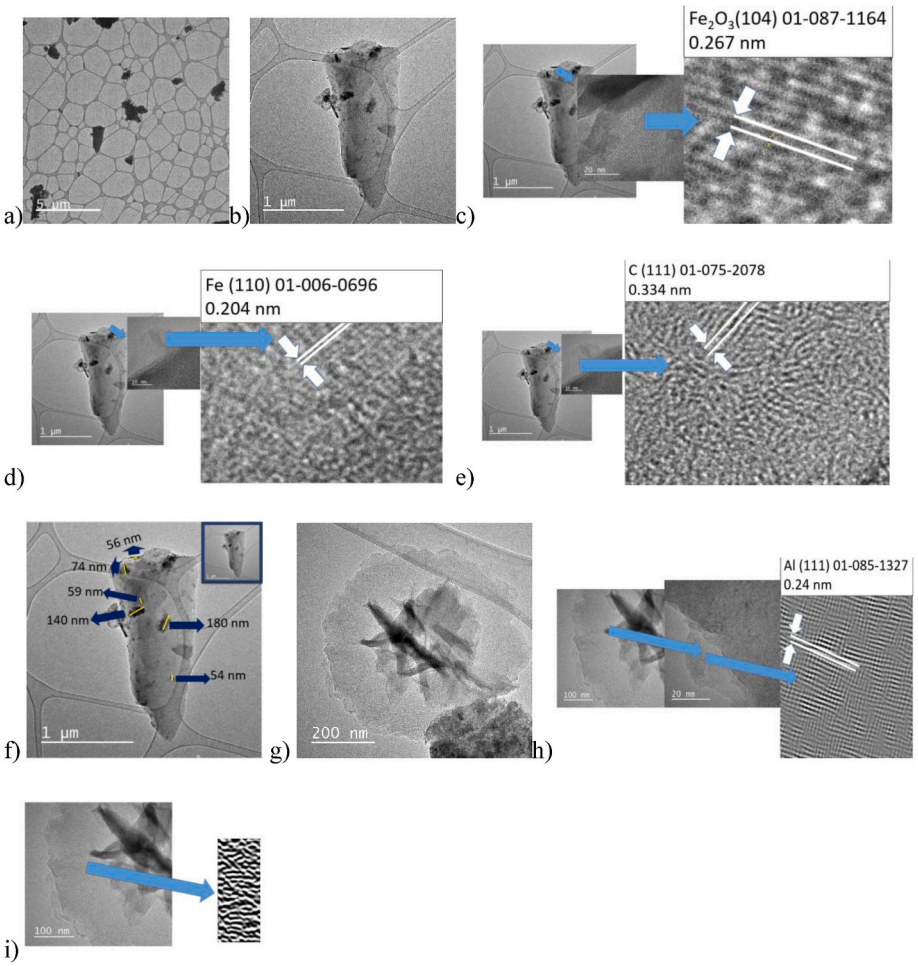

Fig. 4. TEM images a) general view revealing different powder morphologies, b) rod-shape particle, c) Fe_2O_3 (104), d) Fe (110), e) carbon (111), f) demonstration of nanoparticles embedded in the particle g) spherical shaped particle, h) Al (111), ı) amorphous shell.

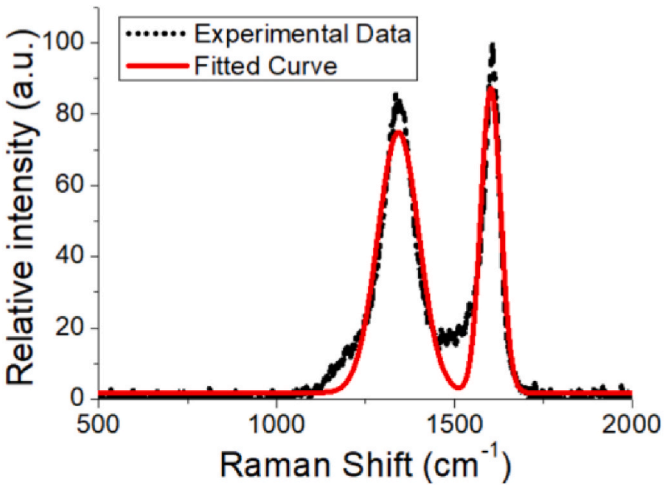

Fig. 5. Raman spectrum of AADC.

When the rate performance of AADC is studied, the electrode exhibits a highly stable performance when the applied current is increased and then decreased over cycles. The superior electrochemical performance depicted in Fig. 6e may be attributed to the high structural stability of the electrode. At 1st discharge, AADC delivers 1246.32 mAh g^{-1} capacity upon the current load of 0.1 A g^{-1}. Then, the same electrode delivers 400 and 350 mAh g^{-1} respectively when 1 A g^{-1} and 2 A h g^{-1} current loads are applied, respectively. Once the applied current is decreased down to 0.1 A g^{-1}, the electrode retains its capacity over 300 cycles. As the electrode conversion kinetics is limited by Li-ion diffusion upon the introduction of Li into the XAZ composite, the lithiation would occur progressively, which will increase the structural stability of the electrode, eventually. Thus, the performance at different rates shows that no delamination or cracking occurs even at high current loads.

In Fig. 7a–d, capacity-voltage curves of AAD, FeDC and AADC are given. Their comparison reveal that no additional plateau and/or trend change noted on the voltage-capacity curvatures of AADC and FeDC confirms the contribution of transition metal oxide is the same and the sulfate remains inactive vs Li.

Kim and Manthriam have stated in their study that the amorphous Al_2O_3 and carbon coating formed here are expected to affect both the formation and growth of SEI, and it is aimed to mechanically strengthen the structure throughout the cycle by forming an active-inactive matrix. Finally, it is expected to contribute to lithium diffusion by restricting electrochemical induced agglomeration in cycling [43].

Fig. 8a–c shows the cyclic voltammetry (CV) curves of FeDC, AAD and AADC. In accordance with studies involving iron and other transition metals as anode materials, peaks around 1.6, 0.9 and 0.6 V are observed in the cathodic region in the first cycle.These peaks are assigned to the reduction of iron oxide and the breakdown of the electrolyte leading to SEI formation on the electrode surface. However, unlike the transition metal oxide samples' CV curves given in our previous study [27], in addition to the curves indicating the oxidation of

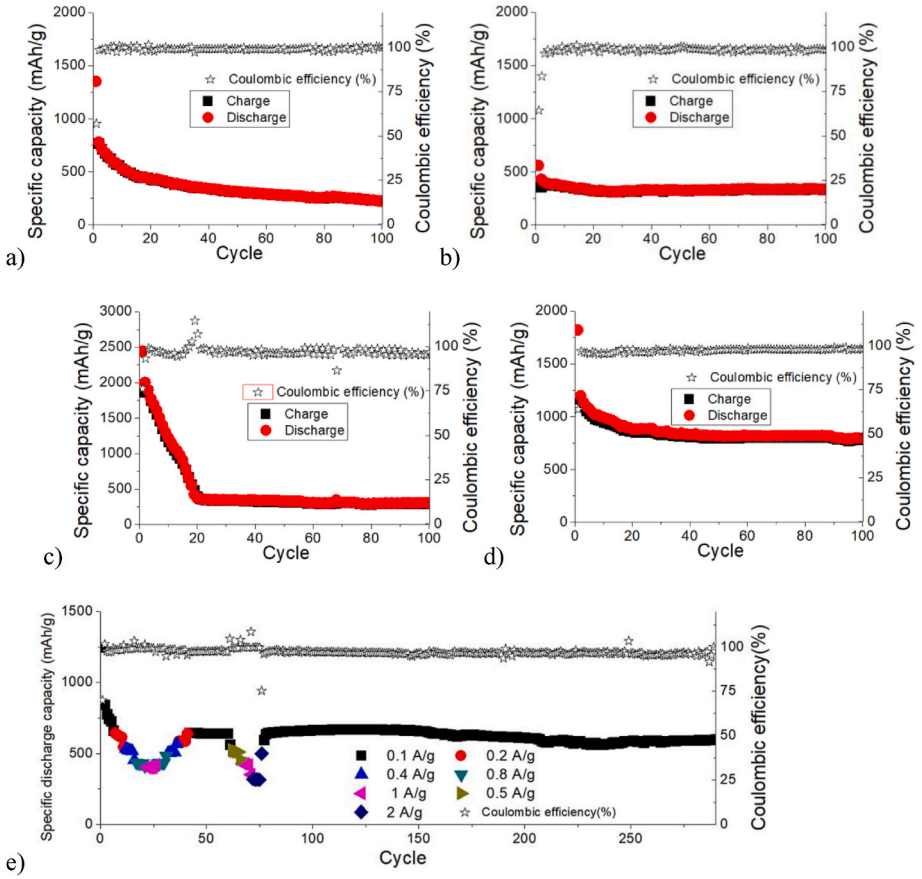

Fig. 6. Galvanostatic performance of a) AAD b) FeDC c) AlC d) AADC between 50 mV and 3 V at the rate of 50 mA g^{-1}. e) The different rate performance of AADC between 50 mV and 3 V.

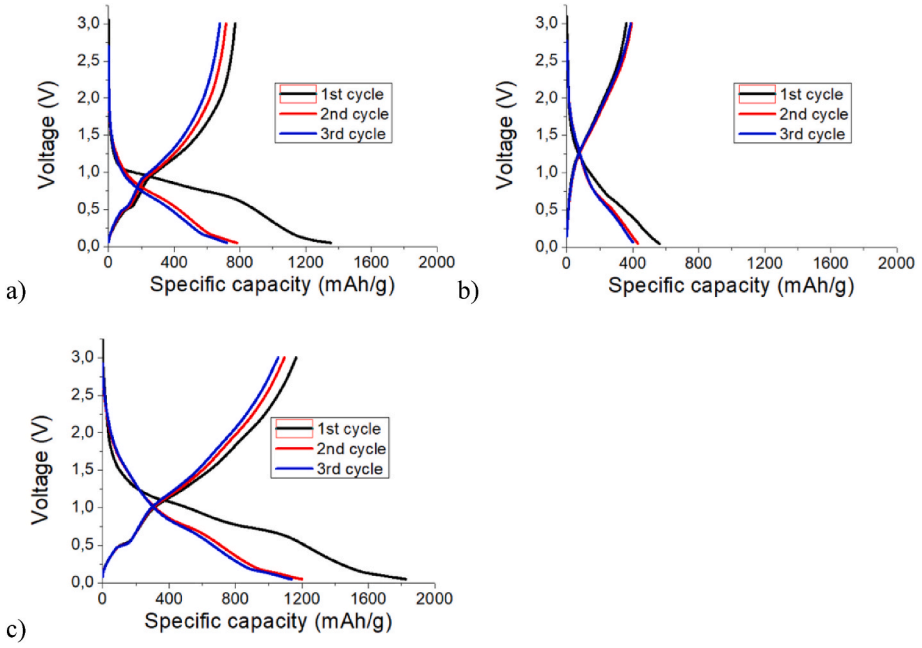

Fig. 7. The Capacity voltage curves (when tested at the rate of 50 mA/g between 50 mV and 3V) of a) AAD, b) FeDC, c) AADC.

metals at 1.4 V, a peak around 0.5 V is also observed. This indicates the reactions related the LiAl phase [17]. In the following cycles, the peak on the cathodic side is shifted from 0.6 V to 0.7 V with polarization. In addition, due to the reduction of metal compounds in the structure, peaks are also observed at 1.5 V on the cathodic side in the following cycles. On the anodic side, no changes are observed in the following cycles. Moreover, FeDC has no cleavage in peaks different form AAD and AADC which is a result from the absence of chromium oxide in the

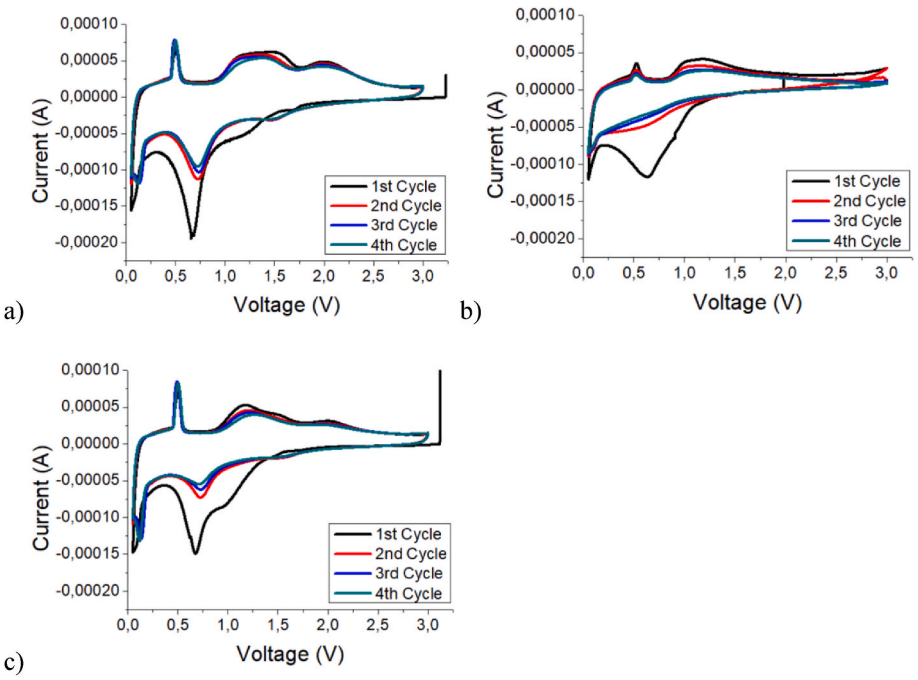

Fig. 8. CV curves for a)FeDC b) AAD c) AADC.

sample. The change in current intensities can be associated with the electrochemical activity of the electrodes [48].

Herein, it is important to note that the existence of Al_2O_3, in XAZ has positive effect on its electrochemical performance since it enables more stable interfacial energy to be obtained as it affects the SEI formation at the electrode/electrolyte interface, hence the cycle retention.

Fig. 9a and b depict the electrochemical impedance spectra of AADC after the 1st and 10th discharge reactions. The EIS spectra of AAD, FeDC and AlC after 1st and 10th discharge reactions, are given as Fig. S4, for comparison. The equivalent circuit model, used to fit the impedance spectra of AADC, is illustrated in the inset of Fig. 9c. Rs represents solution resistance and Rf and Rct represent charge-transfer resistances and CPE1 and CPE2 stand for constant phase elements and W indicates Warburg coefficient which corresponds to the diffusion of Li^+ in the electrode [50,51]. The values (Table 3) show that the cells are well assembled and SEI is well established after 1st discharge reaction [49]. Then , when the Warburg factors (σ) of AADC, AAD, AlC and FeDC at the 1st and the 10th discharged states are studied, (Fig.S5 a-b, Table S1) [51].

Table 3
EIS value according to equivalent circuit.

	1st discharge	10th discharge	Units
Rs	1.098	1.305	Ohm
CPE1	2.48×10^{-5}	2.09×10^{-5}	S^s^a7
a7	7.10×10^{-1}	7.25×10^{-1}	–
Rf	89.12	87.65	Ohm
CPE2	2.00×10^{-2}	1.70×10^{-2}	S^s^a10
a10	7.39×10^{-1}	7.11×10^{-1}	–
W	1.05×10^{-2}	1.56×10^{-2}	S^s^1/2
Rct	35.32	36.64	ohm
Goodness of Fit	4.67×10^{-4}	3.46×10^{-4}	–

the results show that lithium ion diffusion in AADC is easy and diffusion rate changes from 1st to 10th cycle. Possible morphological changes in the electrode upon cycling may explain it [50].

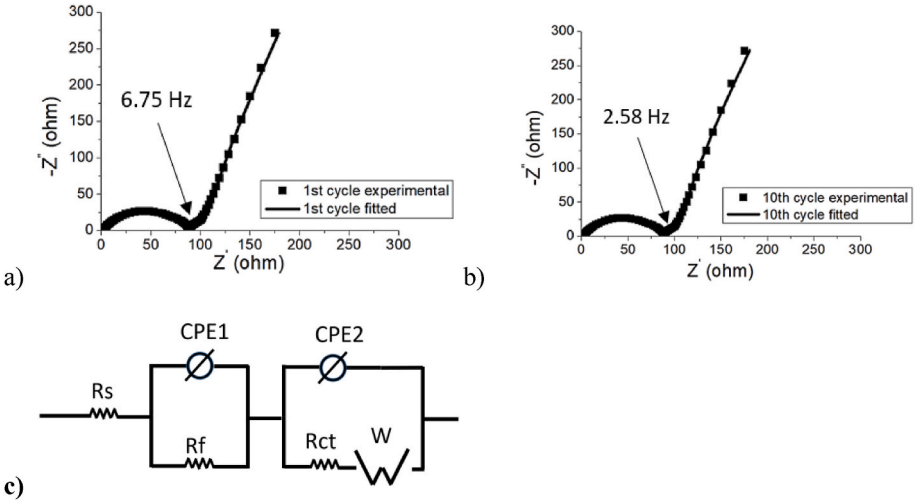

Fig. 9. EIS result after 1st (a) and 10th (b) discharge. c)Equivalent circuit for spectra's.

4. Conclusion

In this study, a domestic (5%C-contained) FeCr alloy is used as a starting material to produce composite with low energy requirement. The electrochemical performances of this composite is studied based on galvanostatic test results. The results are summarized as follows.

- With a correct material selection and process design it is possible to selectively fabricate iron-rich and chromium-rich oxide powders from FeCr alloy.
- In the fabrication of the anode active material a low CO_2 emission is achieved by choosing a locally produced material as the starting material and by using ball milling.
- A heterogeneous composite made of metal/metal oxide/carbon (Metal: Al, Cr, Fe, Co, Mn) is produced by ball milling.
- The composite anode (AADC) with XAZ formula has a higher capacity value than the commercial graphite and LTO. After 100 cycles, AADC delivers 798 mAh g^{-1} under a current load of 50 mA g^{-1}. The rate performance tests further shows that AADC performs 400 mAh g^{-1} capacity value when it is cycled under a current load of 1 A g^{-1}. The same electrode depicts 600 mAh g^{-1}capacities at the 300th cycle under a current load of 100 mA g^{-1}.
- Systematic investigations reveal that the synergitic effect of each component of AADC contributes to its cycle performance.

CRediT authorship contribution statement

Mehmet Feryat Gülcan: Writing – original draft, Visualization, Validation, Investigation. **Billur Deniz Karahan:** Writing – original draft, Validation, Supervision, Methodology, Investigation, Funding acquisition, Conceptualization.

Declaration of competing interest

The authors declare the following financial interests/personal relationships which may be considered as potential competing interests:

Billur Deniz Karahan reports a relationship with Istanbul Medipol University that includes: employment between 2017 and 2022. Istanbul Medipol University sponsored the realization and characterization of the experiments. Istanbul Technical University is the current affiliation of the corresponding author.

The authors would like to greatly acknowledge THE SCIENTIFIC AND TECHNOLOGICAL RESEARCH COUNCIL OF TURKEY (TUBITAK) (Project No: 218M768) for financial support.

The authors thank Eti Krom A.S. for supplying the raw material.

Data availability

No data was used for the research described in the article.

Acknowledgments

The authors would like to greatly acknowledge THE SCIENTIFIC AND TECHNOLOGICAL RESEARCH COUNCIL OF TURKEY (TUBITAK) (Project No: 218M768) for financial support. The authors thank Eti Krom A.S. for supplying the raw material. Moreover, the authors thank Prof. Dr. Sebahattin Gürmen for his support.

Istanbul Medipol University sponsored the realization and characterization of the experiment. Istanbul Technical University is the current affiliation of the corresponding author.

Appendix A. Supplementary data

Supplementary data to this article can be found online at https://doi.org/10.1016/j.matchemphys.2024.129834.

References

[1] H. Yin, Y. Li, Y. Kang, C. Zhang, A two-stage sorting method combining static and dynamic characteristics for retired lithium-ion battery echelon utilization, J. Energy Storage 64 (2023) 107178, https://doi.org/10.1016/j.est.2023.107178.
[2] P.U. Nzereogu, A.D. Omah, F.I. Ezema, E.I. Iwuoha, A.C. Nwanya, Anode materials for lithium-ion batteries: a review, Appl Surf Sci Adv 9 (2022) 100233, https://doi.org/10.1016/j.apsadv.2022.100233.
[3] A. Eftekhari, Low voltage anode materials for lithium-ion batteries, Energy Storage Mater. 7 (2017) 157–180, https://doi.org/10.1016/j.ensm.2017.01.009.
[4] Y. Chen, X. Chen, Y. Zhang, A comprehensive review on metal-oxide nanocomposites for high-performance lithium-ion battery anodes, Energy Fuel. 35 (2021) 6420–6442, https://doi.org/10.1021/acs.energyfuels.1c00315.
[5] N.H. Abdullah, K. Shameli, E.C. Abdullah, L.C. Abdullah, Low cost and efficient synthesis of magnetic iron oxide/activated sericite nanocomposites for rapid removal of methylene blue and crystal violet dyes, Mater. Char. 163 (2020) 110275, https://doi.org/10.1016/j.matchar.2020.110275.
[6] B. Zhao, Y. Zheng, F. Ye, X. Deng, X. Xu, M. Liu, et al., Multifunctional iron oxide nanoflake/graphene composites derived from mechanochemical synthesis for enhanced lithium storage and electrocatalysis, ACS Appl. Mater. Interfaces 7 (2015) 14446–14455, https://doi.org/10.1021/acsami.5b03477.
[7] A. Ali, H. Zafar, M. Zia, I. ul Haq, A.R. Phull, J.S. Ali, et al., Synthesis, characterization, applications, and challenges of iron oxide nanoparticles, Nanotechnol. Sci. Appl. 9 (2016) 49–67, https://doi.org/10.2147/NSA.S99986.
[8] Y. Xu, R. Burns, Z. Liu, Z. Wang, Nanostructure interface for lithium-ion batteries. https://doi.org/10.1016/B978-0-12-814558-6.00002-2, 2019.
[9] H Bin Wu, J.S. Chen, H.H. Hng, X.W. Lou, Nanostructured metal oxide-based materials as advanced anodes for lithium-ion batteries, Nanoscale 4 (2012) 2526–2542, https://doi.org/10.1039/c2nr11966h.
[10] Mumtaz M. Mubasher, N.U.R. Lashari, M. Hassan, S. Tangsee, M.T. Khan, Multi-walled carbon nanotubes and chromium ferrites nanoparticles nanohybrids as anode materials for lithium-ion batteries, J. Alloys Compd. 872 (2021) 159654, https://doi.org/10.1016/j.jallcom.2021.159654.
[11] N. Harpak, G. Davidi, F. Patolsky, Self-transforming stainless-steel into the next generation anode material for lithium ion batteries, J. Energy Chem. 64 (2021) 432–441, https://doi.org/10.1016/j.jechem.2021.05.008.
[12] P.L. Taberna, S. Mitra, P. Poizot, P. Simon, J.M. Tarascon, High rate capabilities Fe3O4-based Cu nano-architectured electrodes for lithium-ion battery applications, Nat. Mater. 5 (2006) 567–573, https://doi.org/10.1038/nmat1672.
[13] Q. Wu, M. Qin, H. Yan, W. Zhong, W. Zhang, M. Liu, et al., Facile replacement reaction enables nano-Ag-decorated three-dimensional Cu foam as high-rate lithium metal anode, ACS Appl. Mater. Interfaces 14 (2022) 42030–42037, https://doi.org/10.1021/acsami.2c10920.
[14] X. Guo, J. Han, L. Zhang, P. Liu, A. Hirata, L. Chen, et al., A nanoporous metal recuperated MnO2 anode for lithium ion batteries, Nanoscale 7 (2015) 15111–15116, https://doi.org/10.1039/c5nr05011a.
[15] C. Cheng, H. Liu, X. Xue, H. Cao, L. Shi, Highly dispersed copper nanoparticle modified nano Li4Ti 5O12 with high rate performance for lithium ion battery, Electrochim. Acta 120 (2014) 226–230, https://doi.org/10.1016/j.electacta.2013.12.049.
[16] X. Chang, Z. Xie, Z. Liu, X. Zheng, J. Zheng, X. Li, Enabling high performance lithium storage in aluminum: the double edged surface oxide, Nano Energy 41 (2017) 731–737, https://doi.org/10.1016/j.nanoen.2017.10.017.
[17] X. Chang, Z. Xie, Z. Liu, X. Zheng, J. Zheng, X. Li, Aluminum: an underappreciated anode material for lithium-ion batteries, Energy Storage Mater. 25 (2020) 93–99, https://doi.org/10.1016/j.ensm.2019.10.027.
[18] A. Vázquez-López, M. García-Carrión, E. Hall, A. Yaseen, I. Kalafat, M. Taeño, et al., Hybrid materials and nanoparticles for hybrid silicon solar cells and Li-ion batteries, J Energy Power Technol 3 (2020) 1, https://doi.org/10.21926/jept.2102020, 1.
[19] J. Kim, W. Jang, J.H. Kim, C.M. Yang, Synthesis of graphene quantum dots-coated hierarchical CuO microspheres composite for use as binder-free anode for lithium-ion batteries, Composites, Part B 222 (2021) 109083, https://doi.org/10.1016/j.compositesb.2021.109083.
[20] S.O. Kim, A. Manthiram, Low-cost carbon-coated Si-Cu3Si-Al2O3 nanocomposite anodes for high-performance lithium-ion batteries, J. Power Sources 332 (2016) 222–229, https://doi.org/10.1016/j.jpowsour.2016.09.089.
[21] J. Leibowitz, E. Allcorn, A. Manthiram, SnSb-TiC-C nanocomposite alloy anodes for lithium-ion batteries, J. Power Sources 279 (2015) 549–554, https://doi.org/10.1016/j.jpowsour.2015.01.055.
[22] E. Allcorn, A. Manthiram, FeSb2–Al2O3–C nanocomposite anodes for lithium-ion batteries, ACS Appl. Mater. Interfaces 6 (2014) 10886–10891, https://doi.org/10.1021/am500448f.
[23] E. Allcorn, A. Manthiram, NiSb–Al2O3–C nanocomposite anodes with long cycle life for Li-ion batteries, J. Phys. Chem. C 118 (2014) 811–822, https://doi.org/10.1021/jp409223c.
[24] D. Applestone, S. Yoon, A. Manthiram, Cu 2Sb-Al 2O 3-C nanocomposite alloy anodes with exceptional cycle life for lithium ion batteries, J. Mater. Chem. 22 (2012) 3242–3248, https://doi.org/10.1039/c2jm13479a.
[25] ALSER MADENCİLİK n.d. https://www.alsermaden.com/Chromium in Turkey and Globe -37-4 (accessed January 14, 2024).
[26] M.F. Gülcan, B.D. Karahan, S. Gürmen, Leaching of iron and chromium from an indigenous ferro chromium alloy via a rotary evaporator: optimum conditions determination and kinetic analysis, J. Mater. Res. Technol. 9 (2020) 14103–14115, https://doi.org/10.1016/j.jmrt.2020.09.133.

[27] M.F. Gülcan, B.D. Karahan, S. Gürmen, Porous, columnar shaped iron rich oxide synthesis for lithium-ion batteries from metallurgical grade, domestic, high carbon ferro-chromium alloys, J. Alloys Compd. 922 (2022) 166215, https://doi.org/10.1016/j.jallcom.2022.166215.
[28] G.R. Hu, J.J. Liu, K. Du, Z.D. Peng, Y.B. Cao, W.G. Wang, et al., Preparing high performance of LiFe(1-x)MxPO 4 by using Fe(1-x)MxC2O4 as raw material precipitated from ferrochrome alloy leaching solution, Phys. B Condens. Matter 446 (2014) 67–70, https://doi.org/10.1016/j.physb.2014.04.040.
[29] M. Khodaei, F. Karimzadeh, M.H. Enayati, Fabrication of iron-alumina nanocomposite powder by high energy ball milling of hematite-aluminum powder mixture, Int. J. Mod. Phys. B 22 (2008) 3233–3236.
[30] V. Rao, A.L. Shashimohan, A.B. Biswas, Studies on the Formation of Y-Fe203 (Maghemite) by Thermal Decomposition of Ferrous Oxalate Dihydrate, vol. 9, 1974.
[31] J.P. Dhal, B.G. Mishra, G. Hota, Ferrous oxalate, maghemite and hematite nanorods as efficient adsorbents for decontamination of Congo red dye from aqueous system, Int. J. Environ. Sci. Technol. 12 (2015) 1845–1856, https://doi.org/10.1007/s13762-014-0535-x.
[32] J. Zeng, C. Peng, R. Wang, C. Cao, X. Wang, J. Liu, Micro-sized FeS2@FeSO4 core-shell composite for advanced lithium storage, J. Alloys Compd. 814 (2020) 1–8, https://doi.org/10.1016/j.jallcom.2019.151922.
[33] N.E. Fouad, S.A. Halawy, M.A. Mohamed, M.I. Zaki, Thermal and spectroscopic studies of chromium chromate hexahydrate - a likely composition for redox surfaces of calcined chromia catalysts, Thermochim. Acta 329 (1999) 23–29, https://doi.org/10.1016/S0040-6031(98)00658-3.
[34] S.A. Halawy, N.E. Fouad, M.A. Mohamed, M.I. Zaki, Kinetic and thermodynamic parameters of the decomposition of chromium chromate in different gas atmospheres, J. Therm. Anal. Calorim. 65 (2001) 167–176, https://doi.org/10.1023/A:1011536920701.
[35] J. Hu, H. Li, X. Huang, L. Chen, Improve the electrochemical performances of Cr2O3 anode for lithium ion batteries, Solid State Ionics 177 (2006) 2791–2799, https://doi.org/10.1016/j.ssi.2006.03.043.
[36] J. Liu, Z. Wang, H. Li, X. Huang, Synthesis and characterization of Cr8O21 as cathode material for rechargeable lithium batteries, Solid State Ionics 177 (2006) 2675–2678, https://doi.org/10.1016/j.ssi.2006.05.017.
[37] S. Yu, B. Guo, T. Zeng, H. Qu, J. Yang, J. Bai, Graphene-based lithium-ion battery anode materials manufactured by mechanochemical ball milling process: a review and perspective, Composites, Part B 246 (2022) 110232, https://doi.org/10.1016/j.compositesb.2022.110232.
[38] K. Chen, R. Huang, F. Gu, Y. Du, Y. Song, A novel hollow Co3O4@N-doped carbon nanobubble film composite for high-performance anode of lithium-ion batteries, Composites, Part B 224 (2021) 109247, https://doi.org/10.1016/j.compositesb.2021.109247.
[39] A.A. Kashale, A.S. Rasal, G.P. Kamble, V.H. Ingole, P.K. Dwivedi, S.J. Rajoba, et al., Biosynthesized Co-doped TiO2 nanoparticles based anode for lithium-ion battery application and investigating the influence of dopant concentrations on its performance, Composites, Part B 167 (2019) 44–50, https://doi.org/10.1016/j.compositesb.2018.12.001.
[40] S. Nam, S. Umrao, S. Oh, K.H. Shin, H.S. Park, I.K. Oh, Sonochemical self-growth of functionalized titanium carbide nanorods on Ti3C2 nanosheets for high capacity anode for lithium-ion batteries, Composites, Part B 181 (2020) 107583, https://doi.org/10.1016/j.compositesb.2019.107583.
[41] K.M. de Souza, M.J.S. de Lemos, Detailed numerical modeling and simulation of Fe2O3−Al thermite reaction. Propellants, Explos Pyrotech 46 (2021) 806–824, https://doi.org/10.1002/prep.202000290.
[42] N.R. Mojarrad, R. Kheirifard, R.T. Mousavian, Y. Afkham, S. Nakisa, Filling ratio of vial: an important parameter for ball milling, J. Therm. Anal. Calorim. 126 (2016) 1097–1103, https://doi.org/10.1007/s10973-016-5635-z.
[43] I.T. Kim, E. Allcorn, A. Manthiram, High-Performance MxSb Al2O3 C M Fe Ni and Cu Nanocomposite-Alloy Anodes for Sodium-Ion (2013) 319–326, https://doi.org/10.1002/ente.201300023.
[44] Y. Jia, Y. Guo, J. Zou, X. Yao, Hydrogenation/dehydrogenation in MgH2-activated carbon composites prepared by ball milling, Int. J. Hydrogen Energy 37 (2012) 7579–7585, https://doi.org/10.1016/j.ijhydene.2012.01.015.
[45] Y. Kashiwaya, K. Ishii, Analysis of the transition state of the carbon and iron oxide mixture activated by mechanical milling, ISIJ Int. 44 (2004) 1981–1990, https://doi.org/10.2355/isijinternational.44.1981.
[46] T.S. Sreeprasad, S.M. Maliyekkal, K.P. Lisha, T. Pradeep, Reduced graphene oxide-metal/metal oxide composites: facile synthesis and application in water purification, J. Hazard Mater. 186 (2011) 921–931, https://doi.org/10.1016/j.jhazmat.2010.11.100.
[47] S. Wu, Y. Jin, D. Wang, Z. Xu, L. Li, X. Zou, et al., Fe2O3/carbon derived from peanut shell hybrid as an advanced anode for high performance lithium ion batteries, J. Energy Storage 68 (2023) 107731, https://doi.org/10.1016/j.est.2023.107731.
[48] T. Kim, W. Choi, H.C. Shin, J.Y. Choi, J.M. Kim, M.S. Park, et al., Applications of voltammetry in lithium ion battery research, J Electrochem Sci Technol 11 (2020) 14–25, https://doi.org/10.33961/jecst.2019.00619.
[49] S.J. An, J. Li, Z. Du, C. Daniel, D.L. Wood, Fast formation cycling for lithium ion batteries, J. Power Sources 342 (2017) 846–852, https://doi.org/10.1016/j.jpowsour.2017.01.011.
[50] Q. Yang, C. Feng, J. Liu, Z. Guo, Synthesis of porous Co 3 O 4/C nanoparticles as anode for Li-ion battery application, Appl. Surf. Sci. 443 (2018) 401–406, https://doi.org/10.1016/j.apsusc.2018.02.230.
[51] H. Mou, S. Chen, W. Xiao, C. Miao, R. Li, G. Xu, et al., Encapsulating homogenous ultra-fine SnO2/TiO2 particles into carbon nanofibers through electrospinning as high-performance anodes for lithium-ion batteries, Ceram. Int. 47 (2021) 19945–19954, https://doi.org/10.1016/j.ceramint.2021.03.329.